This is the accepted manuscript made available via CHORUS. The article has been published as:

Stochastic and mixed density functional theory within the projector augmented wave formalism for simulation of warm dense matter

Vidushi Sharma, Lee A. Collins, and Alexander J. White

Phys. Rev. E **108**, L023201 — Published 1 August 2023

DOI: 10.1103/PhysRevE.108.L023201

Stochastic and Mixed Density Functional Theory within the projector augmented wave formalism for the simulation of warm dense matter

Vidushi Sharma,[1,2] Lee A. Collins,[1] and Alexander J. White[1,*]

[1] *Theoretical Division, Los Alamos National Laboratory, Los Alamos, NM 87545, USA*
[2] *Center for Nonlinear Studies, Los Alamos National Laboratory, Los Alamos, NM 87545, USA*

(Dated: June 2, 2023)

Stochastic and mixed stochastic-deterministic density functional theory (DFT) are promising new approaches for the calculation of the equation-of-state and transport properties in materials under extreme conditions. In the intermediate warm dense matter regime, a state between correlated condensed matter and kinetic plasma, electrons can range from being highly localized around nuclei to delocalized over the whole simulation cell. The plane-wave basis pseudo-potential approach is thus the typical tool of choice for modeling such systems at the DFT level. Unfortunately, stochastic DFT methods scale as the square of the maximum plane-wave energy in this basis. To reduce the effect of this scaling, and improve the overall description of the electrons within the pseudo-potential approximation, we present stochastic and mixed DFT developed and implemented within the projector augmented wave formalism. We compare results between the different DFT approaches for both single-point and molecular dynamics trajectories and present calculations of self-diffusion coefficients of solid density carbon from 1 to 50 eV.

The warm, dense matter (WDM) regime encompasses a wide variety of extreme environments, providing an excellent testing ground for methods that determine material properties. This includes planetary interiors [1–3], stellar systems such as brown and white dwarfs [4], and the capsule compression stage in inertial confinement fusion (ICF) [5–7]. In the ice giant planets, the interiors may support a superionic phase in which hydrogen remains fluid within the lattices of the heavier constituents [8–10], which may help explain the anomalous planetary magnetic fields of Neptune and Uranus. In addition, the difference between an exothermic Neptune and an endothermic Uranus may originate in the nucleation of diamonds from hydrocarbon mixtures [11, 12]. Finally, properties such as equations-of-state and thermal conductivities, of various hydrocarbons determine the performance of ICF capsules irradiated by laser pulses [5], and stopping power characterizes the cooling effects of deposition of the capsule material into the hydrogen fuel [13, 14]. Activation of the James Webb Space Telescope (JWST) presages an explosion in discoveries [15] of exoplanets representing a vast range of physical conditions, distributions, and dynamics involving, to list just a few, surface-atmosphere couplings [16], interfaces between solid and liquid components of interiors [17], and formation pathways [18]. The breakthrough fusion milestone [19] at the National Ignition Facility emphasizes the role played in modeling by ever-improved basic physical attributes. Recent developments signal a pressing need for more accurate microscopic properties over a broad range of WDM conditions.

Many methods exist to determine the basic structure and dynamics of WDM; the most accurate arise from first-principles (FP) techniques such as density functional theory (DFT) [20–22] and path integral Monte Carlo [23, 24], which supply a consistent set of basic material properties as equation-of-state, opacities, mass transport, electrical and thermal conduction. Recently, DFT simulations have provided training information to determine model potentials from machine learning techniques (MLP) [10, 11, 25, 26]. Kohn-Sham (KS) DFT combined with the plane-wave pseudo-potential (PWPP) method is the theory of choice for studying the electronic structure of numerous materials, ranging from solid-state condensed matter to hot dense plasmas. The success of DFT stems from the balance between computational complexity and useful accuracy, achieved by replacing the quantum-mechanical wavefunction by a much simpler quantity: the KS density matrix, typically constructed from the KS Hamiltonian eigenstates.

Cubic scaling of the computational complexity of KS-DFT with respect to both system size and temperature is a major limitation [27]. For WDM systems, orbital-free DFT has been a particularly useful alternative, but it is based on an approximate treatment of the electron non-interacting kinetic energy [28–30]. Linear scaling methods, such as stochastic DFT (sDFT) [31], provide a full KS accuracy alternative for large or hot systems [32]. Mixed stochastic-deterministic DFT (mDFT) shows great promise for providing full KS-DFT accuracy for calculations at any temperature [33]. However, when combined with PWPP method, sDFT, and by extension mDFT, has a quadratic dependence of the computational cost on the maximum plane-wave energy (E_{cut}), *i.e.*, on the grid resolution, compared to standard deterministic DFT's linear dependence. Moreover, it has only been formulated in combination with norm-conserving pseudopotentials, which show either low accuracy or require higher E_{cut}. High accuracy and low E_{cut} can be achieved using soft pseudopotentials, first developed by Vanderbilt [34], leading to a non-orthogonal basis. However, the orbitals from either the norm-conserving or "ultrasoft" pseudopo-

* alwhite@lanl.gov

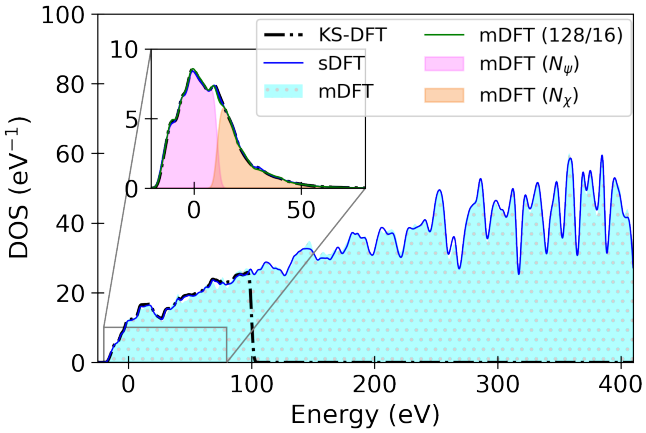


FIG. 1. Disordered 64 carbon system at $(\rho, \mathrm{T}) = (3.52\ \mathrm{g/cc}, 10\ \mathrm{eV})$: Density of states (DOS), and (inset) Occupied DOS, obtained with KS-DFT, sDFT, and mDFT methods. The chemical potential of the system is $\mu = 7.92$ eV. The pink (left) and orange (right) – shaded regions indicate the splitting of deterministic (N_ψ) and stochastic (N_χ) treatments in mDFT.

tentials are not the true KS-orbitals. This is critical for calculation of optical transitions, particularly involving core electrons, *e.g* XANES spectra [35, 36].

The projector augmented wave (PAW) approach, introduced by Blöchl [37] and reformulated by Kresse [38], generalizes the soft pseudopotentials to an "all-electron" formalism. The PAW method provides a realistic description of core electrons, provides access to the full KS-orbitals, has a long and continued history of development, and yields accuracy comparable to more expensive "all-electron" methods [39]. Moreover, it allows for very low E_{cut}, suitable for sDFT/mDFT. In this letter, we develop mDFT, and sDFT by limitation, within the PAW formalism and present isochoric calculations and analysis for carbon spanning the WDM regime, 1 to 50 eV.

Recently, White and Collins [33] proposed the mDFT method that generalizes stochastic and deterministic KS-DFT approaches and improves the computational complexity over a wide range of temperatures. It is based on partitioning the full eigenspectrum of $\widehat{H}_{\mathrm{DFT}}$ into low-energy and high-energy segments such that the maximally occupied low-energy eigenstates ($|\psi\rangle$) are explicitly resolved while the higher-energy states are spanned by random stochastic vectors ($|\chi\rangle$), see Refs. [31, 32, 40–42]. We thus form complementary stochastic vectors (CSV):

$$|\chi'_a\rangle = \Big(\widehat{I} - \sum_{b\in N_\psi} |\psi_b\rangle\langle\psi_b|\Big)|\chi_a\rangle \ , \tag{1}$$

where $|\psi_b\rangle$ is an eigenvector of $\widehat{H}_{\mathrm{DFT}}$ with eigenenergy, ε_b. We define "occupied" CSV's, $X' = f^{\frac{1}{2}}(\widehat{H}_{\mathrm{DFT}})\chi'$, to obtain the mixed density matrix as,

$$\widehat{\rho} = \sum_{a\in N_\chi} |X'_a\rangle\langle X'_a| + \sum_{b\in N_\psi} |\psi_b\rangle f(\varepsilon_b)\langle\psi_b| \ , \tag{2}$$

where f is the Fermi-Dirac operator. KS-DFT and sDFT are respectively limits of mDFT where N_χ or N_ψ are zero. All observables can be expressed as traces over appropriate operators with this density matrix; see [33] for a detailed description.

Fig. 1 shows the density of states (DOS) and occupied DOS for a disordered carbon system, obtained with KS-DFT ($N_\psi = 1024$), sDFT ($N_\chi = 256$) and mDFT ($N_\psi/N_\chi = 128/16$). The low-energy deterministic component of mDFT is shown in pink and there is an overall good agreement across the three methods. The overlap of the components is due to the finite width of Gaussian functions used to define the continuous DOS.

The PAW formalism is based on a linear transformation matrix ($\widehat{\tau}$) connecting the smooth pseudo-density matrix ($\widetilde{\rho}$) to an all-electron density matrix ($\widehat{\rho}$),

$$\widehat{\rho} = \widehat{\tau}\,\widetilde{\rho}\,\widehat{\tau}^\dagger \tag{3}$$

$$\widehat{\tau} = \widehat{I} + \sum_i \big(|\phi_i\rangle - |\tilde{\phi}_i\rangle\big)\langle p_i| \ , \tag{4}$$

with $\langle p_i|\tilde{\phi}_j\rangle = \delta_{ij}$. Here, $|\phi_i\rangle$ is a all-electron partial wave and $|\tilde{\phi}_i\rangle$ is a pseudo partial wave dual to the projector, $|p_i\rangle$. This transformation is exact for a complete set of partial waves and projectors [37, 38]. These functions are limited to localized "augmentation spheres" around each atom. Observables are preserved by defining pseudized operators, $\widetilde{O}$ as:

$$E[\widehat{O}] = \mathrm{Tr}[\widehat{\rho}\,\widehat{O}] = \mathrm{Tr}[\widetilde{\rho}\,\widetilde{O}] \ , \text{with}\ \widetilde{O} = \widehat{\tau}^\dagger\widehat{O}\widehat{\tau} \ . \tag{5}$$

The transformed identity operator gives an $S-$orthogonality condition for the transformed wavefunctions:

$$\widehat{S} = \widehat{\tau}^\dagger\widehat{\tau} = \widehat{I} + \sum_{i,j} |p_i\rangle\big(\langle\phi_i|\phi_j\rangle - \langle\tilde{\phi}_i|\tilde{\phi}_j\rangle\big)\langle p_j| \ , \tag{6}$$

$$\langle\psi_a|\psi_b\rangle = \langle\tilde{\psi}_a|\widehat{S}|\tilde{\psi}_b\rangle = \delta_{ab} \ . \tag{7}$$

Therefore, $\tilde{\psi}_b$ is a solution to the generalized eigenvalue problem, $\widetilde{H}_{\mathrm{KS}}\tilde{\psi} = \varepsilon\widehat{S}\tilde{\psi}$. This $S-$orthogonality condition complicates the generation of transformed stochastic vectors.

Our approximate projections via all-electron / norm-conserving and transformed vectors is given by:

$$\begin{aligned}\widehat{I} &\approx \sum_{a\in N_\chi} |\chi'_a\rangle\langle\chi'_a| + \sum_{b\in N_\psi} |\psi_b\rangle\langle\psi_b| \\ &= \sum_{a\in N_\chi} \widehat{\tau}|\tilde{\chi}'_a\rangle\langle\tilde{\chi}'_a|\widehat{\tau}^\dagger + \sum_{b\in N_\psi} \widehat{\tau}|\tilde{\psi}_b\rangle\langle\tilde{\psi}_b|\widehat{\tau}^\dagger \ .\end{aligned} \tag{8}$$

From the vector transformations, the identity operator, Eq. (8), and the $\widehat{S}$ operator, Eq. (6), we find that

$$\widehat{S} = \widehat{\tau}^\dagger \widehat{I} \widehat{\tau} \approx \widehat{S}\Big(\sum_{a\in N_\chi} |\tilde{\chi}'_a\rangle\langle\tilde{\chi}'_a| + \sum_{b\in N_\psi} |\tilde{\psi}_b\rangle\langle\tilde{\psi}_b|\Big)\widehat{S} \ ,$$
$$\widehat{S}^{-1} \approx \sum_{a\in N_\chi} |\tilde{\chi}'_a\rangle\langle\tilde{\chi}'_a| + \sum_{b\in N_\psi} |\tilde{\psi}_b\rangle\langle\tilde{\psi}_b| \ . \quad (9)$$

For the moment we assume $N_\psi = 0$ and determine the form of $|\tilde{\chi}_a\rangle$. We define a set of stochastic vectors $|\bar{\chi}_a\rangle$ such that $\langle\vec{r}\,|\,\widehat{I}\,|\vec{r}\,'\rangle = \delta(\vec{r},\vec{r}\,') \approx \sum_a \langle\vec{r}\,|\bar{\chi}_a\rangle\langle\bar{\chi}_a|\vec{r}\,'\rangle$, which has the same form as the all-electron stochastic vectors [33], but with $\vec{r}$ and $\vec{r}\,'$ from the coarser grid of the transformed functions [32]. Using the identity $\widehat{I} = \widehat{\tau}\widehat{S}^{-1}\widehat{\tau}^\dagger$ (see Supplemental Material [43], Eq. S8) and Eq. (8), we obtain

$$\widehat{I} \approx \sum_a \widehat{\tau}\widehat{S}^{-\frac{1}{2}}|\bar{\chi}_a\rangle\langle\bar{\chi}_a|\widehat{S}^{-\frac{1}{2}}\widehat{\tau}^\dagger = \sum_a \widehat{\tau}|\tilde{\chi}_a\rangle\langle\tilde{\chi}_a|\widehat{\tau}^\dagger \ ,$$
$$\text{where} \quad |\tilde{\chi}_a\rangle = \widehat{S}^{-\frac{1}{2}}|\bar{\chi}_a\rangle \ . \quad (10)$$

A computationally efficient and sufficiently accurate $\widehat{S}^{-\frac{1}{2}}$ was formulated recently by Li & Neuhauser [44]. Using the same identity, the pseudized density matrix can be written as (see Supplemental Material [43]):

$$\widetilde{\rho} = f(\widehat{S}^{-1}\widetilde{H}_{\rm KS})\widehat{S}^{-1} \ ,$$
$$= f^{\frac{1}{2}}(\widehat{S}^{-1}\widetilde{H}_{\rm KS})\widehat{S}^{-1}f^{\frac{1}{2}}(\widetilde{H}_{\rm KS}\widehat{S}^{-1}) \ . \quad (11)$$

The procedure for PAW mDFT is similar to the all-electron or norm-conserving case [33] with three modifications: (i) the orthogonal stochastic vectors, $\bar{\chi}$, are generated and rotated to the standard PAW frame, $\tilde{\chi}$, (ii) the generalized eigenvalue problem is iteratively solved to obtain $\tilde{\psi}$, (iii) the CSV's are formed via:

$$|\tilde{\chi}'_a\rangle = \Big(\widehat{S}^{-1} - \sum_{b\in N_\psi} |\tilde{\psi}_b\rangle\langle\tilde{\psi}_b|\Big)\widehat{S}|\tilde{\chi}_a\rangle, \text{ giving} \quad (12)$$

$$\widetilde{\rho} = \sum_{a\in N_\chi} |\tilde{X}'_a\rangle\langle\tilde{X}'_a| + \sum_{b\in N_\psi} |\tilde{\psi}_b\rangle f(\varepsilon_b)\langle\tilde{\psi}_b| \ , \text{ with} \quad (13)$$

$$|\tilde{X}'_a\rangle = f^{\frac{1}{2}}(\widehat{S}^{-1}\widetilde{H}_{\rm KS})|\tilde{\chi}'_a\rangle. \quad (14)$$

In Eq. (14), S^{-1} can be applied via the Woodbury formula [45]. The observables necessary to complete the PAW formalism, *e.g.*, on-site density matrix, compensation charge density, can be calculated from Eq. (13). The generalization of PAW forces and stress tensor for mDFT/sDFT is presented in Supplemental Material S2 [43].

Using our open-source [47] PWPP DFT code, `SHRED` (Stochastic and Hybrid Representation Electronic Structure by Density Functional Theory) [48], we perform single-point ground-state energy calculations on 64-atoms disordered carbon at a solid-state density of 3.52 g/cc with the $4e^-$ PAW potential. Figure 2 shows a comparison of the three DFT algorithms in terms of computational time per self consistent field (SCF) cycle on 128 CPUs, and the accuracy and precision of pressure referenced to `SESAME 7833` value [46]. The free energy, pressure and chemical potential for each temperature, along with the combination of orbitals N_ψ/N_χ are listed in Supplemental Material, Table S1 [43]. The combinations range from 136/4 at $k_BT = 1$ eV to 64/40 at $k_BT = 50$ eV; whereas sDFT times are computed with $N_\chi = 128$ for all temperatures. The pressures in sDFT and mDFT, are computed as averages over 10 independent SCF runs using a different set of N_χ stochastic orbitals; with the statistical error (the error bars) expressed as the standard deviation of the sample. The nonlinear nature of the SCF cycle leads to a potential bias in sDFT/mDFT given by the difference between the expected value and the KS-DFT result. Mixed DFT yields energies to within 0.2% (standard deviation of 0.3%) of the reference KS-DFT values with a 42× speedup as compared to KS-DFT at T = 20 eV. Additionally, the chemical potential and pressure are converged to 0.13 eV (standard deviation of 0.18 eV) and 7.27 GPa (standard deviation of 8.29 GPa) relative to their respective KS-DFT results.

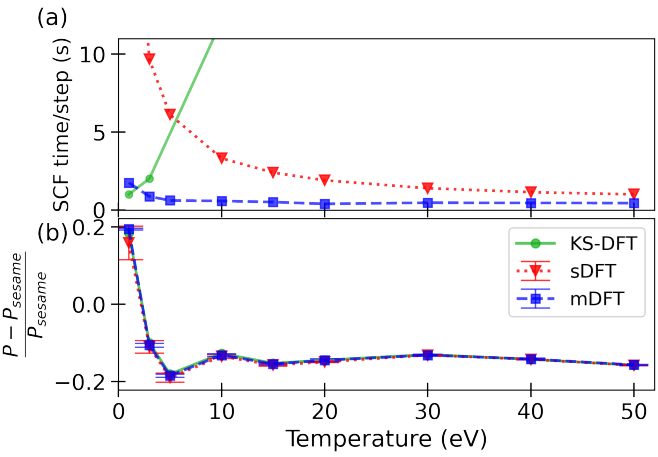


FIG. 2. Disordered 64 carbon snapshot at $\rho = 3.52$ g/cc. Comparison of (a) SCF times per cycle, and (b) relative pressure with reference to `SESAME 7833` ($P_{\rm sesame}$) [46] obtained for Kohn-Sham, stochastic, and mixed DFT calculations.

Electronic nuclear forces depend on the local electronic density and hence do not benefit from the self-averaging effect of sDFT [40]. A comparison of stochastic and mixed DFT forces for several N_ψ/N_χ is presented in Fig. 3, where $F^{i,\psi\chi}_{\alpha,n}$ ($F^{i,\psi}_{\alpha}$) indicates mixed or stochastic (deterministic KS) forces, such that $i = \{x, y, z\}$, $\alpha = 1, \ldots, N_{at}$ indexes the atoms, and $n = 1, \ldots, 10$ indexes the stochastic/mixed run. The absence of an i, n, or α index indicates the magnitude of force, averaged value over 10 independent stochastic/mixed runs, or averaged value over atoms, respectively. The standard deviation over n independent runs averaged over the atoms, is given by:

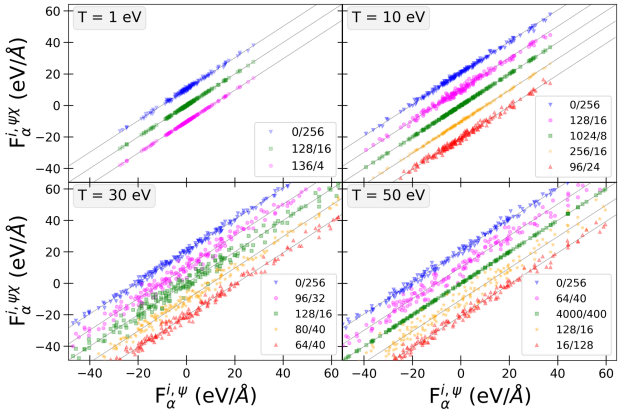


FIG. 3. Comparison of mixed ($\mathrm{F}_\alpha^{i,\psi\chi}$) vs Kohn-Sham ($\mathrm{F}_\alpha^{i,\psi}$) DFT components of forces on all atoms obtained for various N_ψ/N_χ. The agreement between stochastic (0/256, blue triangles) and deterministic forces improves at higher temperatures. The data points shown in magenta circles represent the chosen N_ψ/N_χ for mixed DFT calculations at a given temperature. At higher temperatures, the area of the force plots is zoomed in to keep a constant scale. The order of lines at each T matches the key.

$$\sigma^{\psi\chi} = \sum_{\alpha=1}^{N_{at}} N_{at}^{-1} \sqrt{\sum_{n=1}^{10} \frac{(\mathrm{F}_{\alpha,n}^{\psi\chi} - \mathrm{F}_\alpha^{\psi})^2}{10}} \; ; \qquad (15)$$

also see Supplemental Material, Table S2 [43]. Upon comparing the bias in mixed forces ($|\mathrm{F}^{\psi\chi} - \mathrm{F}^{\psi}|$) with the statistical error ($\sigma^{\psi\chi}$), one finds that the largest magnitude of the force bias across temperatures is 1.280 eV/Å, which is smaller than the largest magnitude of the statistical error, 10.471 eV/Å, as expected [50].

Figure 3 shows a comparison of the components of mDFT and sDFT forces ($\mathrm{F}_\alpha^{i,\psi\chi}$) obtained for several N_ψ/N_χ with the Kohn-Sham forces ($\mathrm{F}_\alpha^{i,\psi}$). The displacement in the mixed forces about the linear curve indicates a statistical error that diminishes with an increasing N_χ at higher temperatures. At a given temperature, the data points shown in magenta (circles) indicate the mixed forces for N_ψ/N_χ employed elsewhere in this work. The forces at T = (30, 50) eV, are in good agreement between mDFT and KS-DFT with a standard deviation of 8.647 eV/Å and 10.364 eV/Å respectively. These can be viewed in conjunction with the purely stochastic forces shown in blue. At lower temperatures, increasing the number of deterministic KS-orbitals reduces the fluctuations in forces, *e.g.*, at T = 10 eV, increasing N_ψ from 128/16 (magenta circles) to 256/16 (yellow stars) improves the distribution of forces significantly. However, at moderate to high temperatures one would require a drastically large N_ψ to obtain accurate forces, see T = 50 eV, Fig. 3. Hence it is advantageous to increase N_χ's and decrease N_ψ as the temperature increases [33], as evidenced from the forces obtained with N_ψ/N_χ = 128/16 vs. 16/128 at T = 50 eV.

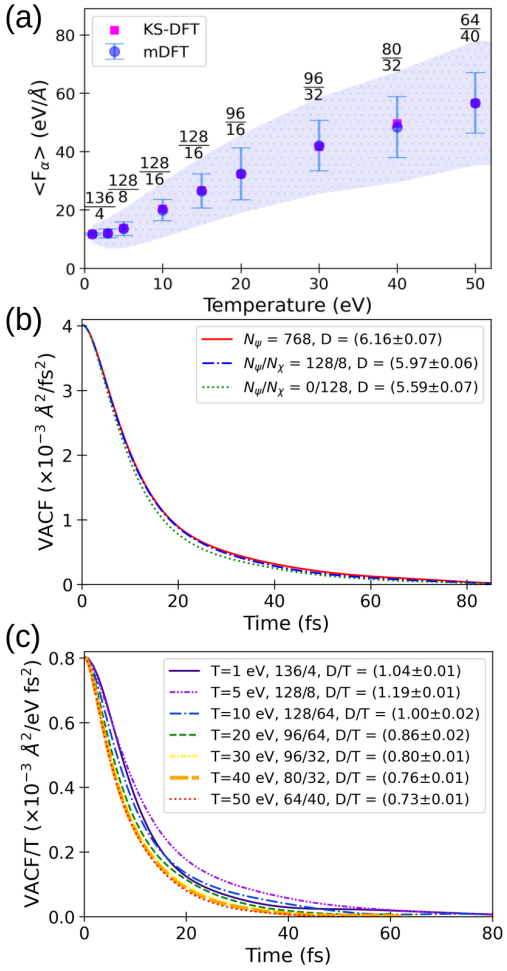


FIG. 4. Disordered 64 carbon system at $\rho = 3.52$ g/cc: average magnitude of force on atoms $\langle \mathrm{F}_\alpha \rangle$ obtained with KS- and mixed DFT for a single snapshot. For KS-DFT, N_ψ ranges from 256 at T = 1 eV to 6400 at T = 50 eV. The error bars indicate the statistical error over mixed DFT runs, and the shaded region represents a Langevin-type friction term at the respective temperature, $\langle \mathrm{F}_\alpha \rangle \pm 2\varsigma$ with $\gamma_\alpha = 0.04$ fs^{-1} [49]. A comparison of (b) velocity autocorrelation function (VACF) for KS (solid line), mixed (dash-dot line) and stochastic (dotted line) DFT methods at T=5 eV, and (c) VACF/T at different temperatures (T). The self-diffusion coefficients (D, integral of VACF) are given in the key with units of 10^{-3} cm^2/s.

The magnitude of force averaged over all atoms $\langle \mathrm{F}_\alpha \rangle$ is computed with mixed and KS-DFT methods, as shown in Fig. 4(a). The error bars denote the standard deviation in the mDFT forces, $\sigma^{\psi\chi}$, and the blue-shaded band indicates a thermal fluctuation region described by a Langevin-type fluctuation ς, such that

$$m_\alpha \ddot{q}_\alpha = f_\alpha - \gamma_\alpha p_\alpha + \varsigma \eta_\alpha(t) \; , \qquad (16)$$

where $\varsigma \equiv \sqrt{2 m_\alpha \gamma_\alpha k_B T}$, (q_α, p_α) are the coordinates and momenta of the atoms, f_α is the force on the atom, γ_α is the damping constant, and $\eta_\alpha(t)$ is a Gaussian process such that $\langle \eta_\alpha(t) \rangle = 0$ and $\langle \eta_\alpha(t) \eta_{\alpha'}(t') \rangle = \delta_{\alpha\alpha'} \delta(t - t')$.

Langevin molecular dynamics was successfully used to investigate forces from sDFT–based simulations [49, 50]. At a given temperature, $\langle F_\alpha \rangle \pm 2\varsigma$ is explicitly computed and interpolated to yield the thermal-fluctuation band in Fig. 4(a). The averaged mDFT forces along with the error bars are contained within the thermal band. This shows that the statistical error as captured quantitatively by $\sigma^{\psi\chi}$, and qualitatively in Fig. 3, can be absorbed by the thermal fluctuations in dynamical simulations. While the statistical fluctuations are contained within 2ς, the bias in the forces lies within 1ς indicating that accuracy converges faster than precision [32].

In order to investigate the effect of these relatively small biases on observables, we apply mDFT to compute transport properties via molecular dynamics (MD) simulations. We employ an isokinetic [51] ensemble that is typically used for WDM transport calculations [29, 30]. The time-averaged free energy and total pressure along with their standard deviations are given in Supplemental Material, Table S3 [43]. We compute the velocity autocorrelation function (VACF) and self-diffusion coefficient (D) [29, 30, 52] of carbon with KS-, mixed and stochastic DFT, see Fig. 4(b). The finite simulation time in MD results in a statistical error, in addition to that due to the stochasticity in sDFT and mDFT. We see the average mDFT diffusion coefficients falls between 1 and 2 times the statistical error estimate, which is within the range of reasonable estimates, see Supplemental Material [43]. The pure sDFT diffusion coefficient falls slightly outside this range, but is still within 10% of the deterministic case.

Figure 4(c) shows a comparison of temperature-scaled VACF and D for several T, with the N_ψ/N_χ specified in the key. The relationship between D and T over a temperature range at any given density was previously investigated for high-Z materials that exhibit multiple ionization states [53]. It was argued that, over a large temperature and density range, the mutually compensating effects of increased ionization and thermal energy result in a constant coupling parameter Γ, giving rise to a so-called $\Gamma-$plateau which, in turn, affects quantities such as self-diffusion and viscosity. We see that for 1 to 5 eV the change in temperature dominates correlation, leading to an increase in D/T, while for greater than 5 eV the ionization effects become significant leading to a decrease in D/T.

We have presented the first implementation of the mDFT and sDFT methods within the plane-wave PAW formalism for DFT. The PAW formalism provides a significant acceleration of stochastic DFT methods due to both smaller grids and decreased eigenspectrum range. Additionally it opens the door to efficient, all-electron accuracy, calculations of matter in extreme conditions, as is possible in ambient conditions [39]. We have demonstrated the efficacy of this approach in the simulation of transport properties in isochorically heated warm dense carbon up to 50 eV, observing the crossover from kinetically to Coulomb-dominated correlation effects. Future work will include additional transport studies, and application of the PAW method to time-dependent mDFT and optical response via the Kubo-Greenwood approach.

ACKNOWLEDGMENTS

This work was supported by the U.S. Department of Energy through the Los Alamos National Laboratory (LANL). Research presented in this article was supported by the Laboratory Directed Research and Development program of LANL, under project number 20210233ER, and Science Campaign 4. We acknowledge the support of the Center for Nonlinear Studies (CNLS). This research used computing resources provided by the LANL Institutional Computing and Advanced Scientific Computing programs. Los Alamos National Laboratory is operated by Triad National Security, LLC, for the National Nuclear Security Administration of U.S. Department of Energy (Contract No. 89233218CNA000001).

[1] National Academies of Sciences, Engineering, and Medicine, *Exoplanet Science Strategy* (The National Academies Press, Washington, DC, 2018).

[2] M. Bethkenhagen, E. R. Meyer, S. Hamel, N. Nettelmann, M. French, L. Scheibe, C. Ticknor, L. A. Collins, J. D. Kress, J. J. Fortney, and R. Redmer, Planetary Ices and the Linear Mixing Approximation, The Astrophysical Journal **848**, 67 (2017).

[3] N. A. Teanby, P. G. J. Irwin, J. I. Moses, and R. Helled, Neptune and Uranus: ice or rock giants?, Philosophical Transactions of the Royal Society A: Mathematical, Physical and Engineering Sciences **378**, 20190489 (2020).

[4] A. Becker, M. Bethkenhagen, C. Kellermann, J. Wicht, and R. Redmer, Material Properties for the Interiors of Massive Giant Planets and Brown Dwarfs, The Astronomical Journal **156**, 149 (2018).

[5] S. X. Hu, L. A. Collins, T. R. Boehly, Y. H. Ding, P. B. Radha, V. N. Goncharov, V. V. Karasiev, G. W. Collins, S. P. Regan, and E. M. Campbell, A review on ab initio studies of static, transport, and optical properties of polystyrene under extreme conditions for inertial confinement fusion applications, Physics of Plasmas **25**, 056306 (2018).

[6] A. Fernandez-Pañella, M. Millot, D. E. Fratanduono, M. P. Desjarlais, S. Hamel, M. C. Marshall, D. J. Erskine, P. A. Sterne, S. Haan, T. R. Boehly, G. W. Collins, J. H. Eggert, and P. M. Celliers, Shock Compression of Liquid Deuterium up to 1 TPa, Phys. Rev. Lett. **122**, 255702 (2019).

[7] B. Bachmann, S. A. MacLaren, S. Bhandarkar, T. Briggs, D. Casey, L. Divol, T. Döppner, D. Fittinghoff, M. Freeman, S. Haan, G. N. Hall, *et al.*, Measurement of Dark Ice-Ablator Mix in Inertial Confinement Fusion, Phys. Rev. Lett. **129**, 275001 (2022).

[8] M. Millot, S. Hamel, J. R. Rygg, P. M. Celliers, G. W. Collins, F. Coppari, D. E. Fratanduono, R. Jeanloz, D. C. Swift, and J. H. Eggert, Experimental evidence for superionic water ice using shock compression, Nature Physics **14**, 297 (2018).

[9] B. Cheng, M. Bethkenhagen, C. J. Pickard, and S. Hamel, Phase behaviours of superionic water at planetary conditions, Nature Physics **17**, 1228 (2021).

[10] H. Gao, C. Liu, J. Shi, S. Pan, T. Huang, X. Lu, H.-T. Wang, D. Xing, and J. Sun, Superionic Silica-Water and Silica-Hydrogen Compounds in the Deep Interiors of Uranus and Neptune, Phys. Rev. Lett. **128**, 035702 (2022).

[11] B. Cheng, S. Hamel, and M. Bethkenhagen, Diamond formation from hydrocarbon mixtures in planets (2022).

[12] M. Ross, The ice layer in Uranus and Neptune – diamonds in the sky?, Nature **292**, 435 (1981).

[13] A. J. White, O. Certik, Y. H. Ding, S. X. Hu, and L. A. Collins, Time-dependent orbital-free density functional theory for electronic stopping power: Comparison to the Mermin-Kohn-Sham theory at high temperatures, Phys. Rev. B **98**, 144302 (2018).

[14] Y. H. Ding, A. J. White, S. X. Hu, O. Certik, and L. A. Collins, Ab Initio Studies on the Stopping Power of Warm Dense Matter with Time-Dependent Orbital-Free Density Functional Theory, Phys. Rev. Lett. **121**, 145001 (2018).

[15] E.-M. Ahrer, L. Alderson, N. M. Batalha, N. E. Batalha, J. L. Bean, T. G. Beatty, T. J. Bell, B. Benneke, Z. K. Berta-Thompson, A. L. Carter, I. J. M. Crossfield, *et al.*, Identification of carbon dioxide in an exoplanet atmosphere, Nature (2022).

[16] W. Dietrich, S. Kumar, A. J. Poser, M. French, N. Nettelmann, R. Redmer, and J. Wicht, Magnetic induction processes in hot Jupiters, application to KELT-9b, Monthly Notices of the Royal Astronomical Society **517**, 3113 (2022).

[17] Y. Miyazaki and D. J. Stevenson, A Subsurface Magma Ocean on Io: Exploring the Steady State of Partially Molten Planetary Bodies, The Planetary Science Journal **3**, 256 (2022).

[18] S.-F. Liu, Y. Hori, S. Müller, X. Zheng, R. Helled, D. Lin, and A. Isella, The formation of Jupiter's diluted core by a giant impact, Nature **572**, 355 (2019).

[19] A. B. Zylstra, O. A. Hurricane, D. A. Callahan, A. L. Kritcher, J. E. Ralph, H. F. Robey, J. S. Ross, C. V. Young, K. L. Baker, D. T. Casey, T. Döppner, *et al.*, Burning plasma achieved in inertial fusion, Nature **601**, 542 (2022).

[20] W. Kohn and L. J. Sham, Self-Consistent Equations Including Exchange and Correlation Effects, Phys. Rev. **140**, A1133 (1965).

[21] A. Pribram-Jones, S. Pittalis, E. K. U. Gross, and K. Burke, Thermal Density Functional Theory in Context, in *Frontiers and Challenges in Warm Dense Matter*, edited by F. Graziani, M. P. Desjarlais, R. Redmer, and S. B. Trickey (Springer International Publishing, Cham, 2014) pp. 25–60.

[22] M. Bonitz, T. Dornheim, Z. A. Moldabekov, S. Zhang, P. Hamann, H. Kählert, A. Filinov, K. Ramakrishna, and J. Vorberger, Ab initio simulation of warm dense matter, Physics of Plasmas **27**, 042710 (2020).

[23] D. M. Ceperley, Path integrals in the theory of condensed helium, Rev. Mod. Phys. **67**, 279 (1995).

[24] K. P. Driver and B. Militzer, All-Electron Path Integral Monte Carlo Simulations of Warm Dense Matter: Application to Water and Carbon Plasmas, Phys. Rev. Lett. **108**, 115502 (2012).

[25] V. L. Deringer, M. A. Caro, and G. Csányi, Machine Learning Interatomic Potentials as Emerging Tools for Materials Science, Advanced Materials **31**, 1902765 (2019).

[26] H.-F. Li, A. R. Oganov, H. Cui, X.-F. Zhou, X. Dong, and H.-T. Wang, Ultrahigh-Pressure Magnesium Hydrosilicates as Reservoirs of Water in Early Earth, Phys. Rev. Lett. **128**, 035703 (2022).

[27] A. Blanchet, M. Torrent, and J. Clérouin, Requirements for very high temperature Kohn–Sham DFT simulations and how to bypass them, Physics of Plasmas **27**, 122706 (2020).

[28] F. Lambert, J. Clérouin, and S. Mazevet, Structural and dynamical properties of hot dense matter by a Thomas-Fermi-Dirac molecular dynamics, Europhysics Letters **75**, 681 (2006).

[29] C. Ticknor, J. D. Kress, L. A. Collins, J. Clérouin, P. Arnault, and A. Decoster, Transport properties of an asymmetric mixture in the dense plasma regime, Phys. Rev. E **93**, 063208 (2016).

[30] A. J. White, L. A. Collins, J. D. Kress, C. Ticknor, J. Clérouin, P. Arnault, and N. Desbiens, Correlation and transport properties for mixtures at constant pressure and temperature, Phys. Rev. E **95**, 063202 (2017).

[31] M. D. Fabian, B. Shpiro, E. Rabani, D. Neuhauser, and R. Baer, Stochastic density functional theory, WIREs Computational Molecular Science **9**, e1412 (2019).

[32] Y. Cytter, E. Rabani, D. Neuhauser, and R. Baer, Stochastic density functional theory at finite temperatures, Phys. Rev. B **97**, 115207 (2018).

[33] A. J. White and L. A. Collins, Fast and Universal Kohn-Sham Density Functional Theory Algorithm for Warm Dense Matter to Hot Dense Plasma, Phys. Rev. Lett. **125**, 055002 (2020).

[34] K. Laasonen, A. Pasquarello, R. Car, C. Lee, and D. Vanderbilt, Car-Parrinello molecular dynamics with Vanderbilt ultrasoft pseudopotentials, Phys. Rev. B **47**, 10142 (1993).

[35] M. Taillefumier, D. Cabaret, A.-M. Flank, and F. Mauri, X-ray absorption near-edge structure calculations with the pseudopotentials: Application to the k edge in diamond and α-quartz, Phys. Rev. B **66**, 195107 (2002).

[36] N. Brouwer, V. Recoules, N. Holzwarth, and M. Torrent, Calculation of optical properties with spin-orbit coupling for warm dense matter, Computer Physics Communications **266**, 108029 (2021).

[37] P. E. Blöchl, Projector augmented-wave method, Phys. Rev. B **50**, 17953 (1994).

[38] G. Kresse and D. Joubert, From ultrasoft pseudopotentials to the projector augmented-wave method, Phys. Rev. B **59**, 1758 (1999).

[39] K. Lejaeghere, G. Bihlmayer, T. Björkman, P. Blaha, S. Blügel, V. Blum, D. Caliste, I. E. Castelli, S. J. Clark, A. D. Corso, S. de Gironcoli, *et al.*, Reproducibility in density functional theory calculations of solids, Science **351**, aad3000 (2016).

[40] R. Baer, D. Neuhauser, and E. Rabani, Self-Averaging Stochastic Kohn-Sham Density-Functional Theory, Phys. Rev. Lett. **111**, 106402 (2013).

[41] D. Neuhauser, R. Baer, and E. Rabani, Communication:

Embedded fragment stochastic density functional theory, The Journal of Chemical Physics **141**, 041102 (2014).
[42] R. Baer, D. Neuhauser, and E. Rabani, Stochastic Vector Techniques in Ground-State Electronic Structure, Annual Review of Physical Chemistry **73**, 255 (2022).
[43] See Supplemental Material at [URL] for the derivation of identity operator, density matrix, stress tensor, and forces in PAW formalism; combination of mixed deterministic-stochastic orbitals, magnitude of forces and stochastic errors, energies and pressures in molecular dynamics along with their standard deviations, and error estimation procedure for the velocity autocorrelation function. The Supplemental Material also includes Refs. [54–57].
[44] W. Li and D. Neuhauser, Real-space orthogonal projector-augmented-wave method, Phys. Rev. B **102**, 195118 (2020).
[45] A. Levitt and M. Torrent, Parallel eigensolvers in plane-wave Density Functional Theory, Computer Physics Communications **187**, 98 (2015).
[46] B. Bennett, J. Johnson, G. Kerley, and G. Rood, Recent Developments in the Sesame Equation-Of-State Library, Los Alamos National Laboratory LA-7130 10.2172/5150206 (1978).
[47] A. White, https://github.com/lanl/shred (2023).
[48] SHRED: Stochastic and Hybrid Representation Electronic structure by Density functional theory, a plane-wave DFT code employing Kohn-Sham, orbital-free, stochastic, and mixed stochastic-deterministic DFT methods.
[49] E. Arnon, E. Rabani, D. Neuhauser, and R. Baer, Efficient Langevin dynamics for "noisy" forces, The Journal of Chemical Physics **152**, 161103 (2020).
[50] B. Shpiro, M. D. Fabian, E. Rabani, and R. Baer, Forces from Stochastic Density Functional Theory under Nonorthogonal Atom-Centered Basis Sets, Journal of Chemical Theory and Computation **18**, 1458 (2022).
[51] P. Minary, G. J. Martyna, and M. E. Tuckerman, Algorithms and novel applications based on the isokinetic ensemble. II. Ab initio molecular dynamics, The Journal of Chemical Physics **118**, 2527 (2003).
[52] E. R. Meyer, J. D. Kress, L. A. Collins, and C. Ticknor, Effect of correlation on viscosity and diffusion in molecular-dynamics simulations, Phys. Rev. E **90**, 043101 (2014).
[53] J. Clérouin, G. Robert, P. Arnault, J. D. Kress, and L. A. Collins, Behavior of the coupling parameter under isochoric heating in a high-Z plasma, Phys. Rev. E **87**, 061101 (2013).
[54] M. Torrent, F. Jollet, F. Bottin, G. Zérah, and X. Gonze, Implementation of the projector augmented-wave method in the ABINIT code: Application to the study of iron under pressure, Computational Materials Science **42**, 337 (2008).
[55] T. Rangel, D. Caliste, L. Genovese, and M. Torrent, A wavelet-based Projector Augmented-Wave (PAW) method: Reaching frozen-core all-electron precision with a systematic, adaptive and localized wavelet basis set, Computer Physics Communications **208**, 1 (2016).
[56] A. H. Romero, D. C. Allan, B. Amadon, G. Antonius, T. Applencourt, L. Baguet, J. Bieder, F. Bottin, J. Bouchet, E. Bousquet, F. Bruneval, *et al.*, ABINIT: Overview and focus on selected capabilities, The Journal of Chemical Physics **152**, 124102 (2020).
[57] S. Lehtola, C. Steigemann, M. J. Oliveira, and M. A. Marques, Recent developments in LIBXC – A comprehensive library of functionals for density functional theory, SoftwareX **7**, 1 (2018).